J|A|C|S
ARTICLES
Published on Web 07/28/2005

Tailoring the Optical Property by a Three-Dimensional Epitaxial Heterostructure: A Case of ZnO/SnO_2

Qin Kuang, Zhi-Yuan Jiang, Zhao-Xiong Xie,* Shui-Chao Lin, Zhi-Wei Lin, Su-Yuan Xie, Rong-Bin Huang, and Lan-Sun Zheng

Contribution from the State Key Laboratory for Physical Chemistry of Solid Surfaces and Department of Chemistry, Xiamen University, Xiamen 361005, China

Received April 8, 2005; E-mail: zxxie@xmu.edu.cn

Abstract: Epitaxial growth, as a best strategy to attain a heterostructure with a well-defined and clean interface, usually takes place on a planar substrate. In this paper, using a ZnO/SnO_2 core−shell heterostructure as an example, we demonstrate the possibility of establishing a three-dimensional epitaxial interface between two materials with different crystal systems for the first time and show possible tailoring optical properties by building the heteroepitaxial crystal interface. The characterization results of element mapping, high-resolution transmission electron microscopy, and selected area electric diffraction reveal that the as-prepared ZnO/SnO_2 heterostructure has a tetrapod-like ZnO core and a SnO_2 shell with 15−30 nm, and their special epitaxial relation is $(010)_{SnO_2}||(0\bar{1}10)_{ZnO}$ and $[100]_{SnO_2}||[0001]_{ZnO}$. Such three-dimensional epitaxy between the ZnO core and SnO_2 shell is quite different from the usual planar epitaxy or three-dimensional epitaxy between materials having the same crystal structure. A rational model of such complicated epitaxy has been proposed through investigating the certain structural comparability between the wurtzite ZnO and rutile SnO_2 crystals. The as-prepared T-ZnO/SnO_2 epitaxial heterostructure exhibits unique luminescence properties in contrast with individual tetrapod ZnO and SnO_2 nanostructures, in which the epitaxial interface induces new luminescence properties. This result may inspire great interest in exploring other complicated epitaxy systems and their potential applications in laser, gas sensor, solar energy conversion, photo catalysis, and nanodevices in the future.

1. Introduction

Composition-modulated heterostructure nanomaterials display high versatility and applicability as building blocks in nanoscale electronics and photonics,[1] which have recently directed considerable research efforts on the synthesis and manufacturing of various heterostructures such as nanowires with superlattice structures[2−4] and coaxial[5−12] or biaxial nanocables.[13−17] A key factor that affects the performance and reliability of a nanodevice made of heterostructure nanomaterials is the quality of the heterostructure interface, since defects at the interface would deteriorate device characteristics.[18] To attain the heterostructure with the well-defined and clean interface, the epitaxial growth has long been regarded as the best strategy. Epitaxial growth, however, usually takes place two-dimensionally on a planar substrate or, recently, was built three-dimensionally on the nanowire surfaces between two materials with the same crystal structure.[7−11,18] In this paper, using the epitaxial growth of a SnO_2 shell on tetrapod ZnO core as an example, we demonstrate the possibility of establishing three-dimensional epitaxial interface between two materials with different crystal systems for the first time and show the possible tailoring optical properties by building a heteroepitaxial crystal interface.

ZnO and SnO_2, well-known wide direct band-gap ($E_g = 3.37$ and 3.6 eV at 300 K, respectively) semiconductors, have been considered as the most promising functional materials due to their highly sensitive gas sensing and excellent optical properties. Recently, many studies have proved that composite materials

(1) Park, W. I.; Yi, G. C.; Kim, M.; Pennycook, S. J. *Adv. Mater.* **2003**, *15*, 256−259.
(2) Wu, Y. Y.; Fan, R.; Yang, P. D. *Nano Lett.* **2002**, *2*, 83−86.
(3) Gudiksen, M. S.; Lauhon, L. J.; Wang, J. F.; Smith, D. C.; Lieber, C. M. *Nature* **2002**, *415*, 617−620.
(4) Solanki, R.; Huo, J.; Freeouf, J. L.; Miner, B. *Appl. Phys. Lett.* **2002**, *81*, 3864−3866.
(5) Suenaga, K.; Colliex, C.; Demoncy, N.; Loiseau, A.; Pascard, H.; Willaime, F. *Science* **1997**, *278*, 653−655.
(6) Zhang, Y.; Suenaga, K.; Colliex, C.; Iijima, S. *Science* **1998**, *281*, 973−975.
(7) Han, S.; Li, C.; Liu, Z. Q.; Lei, B.; Zhang, D. H.; Jin, W.; Liu, X. L.; Tang, T.; Zhou, C. W. *Nano Lett.* **2004**, *4*, 1241−1246.
(8) Lauhon, L. J.; Gudiksen, M. S.; Wang, D. L.; Lieber, C. M. *Nature* **2002**, *420*, 57−61.
(9) (a)Kong, X. Y.; Ding, Y.; Wang, Z. L. *J. Phys. Chem. B* **2004**, *108*, 570−574. (b) Hu, J. Q.; Li, Q.; Meng, X. M.; Lee, C. S.; Lee, S. T. *Chem. Mater.* **2003**, *15*, 305−308.
(10) Li, Y. B.; Bando, Y.; Golberg, D. *Chem. Phys. Lett.* **2003**, *375*, 102−105.
(11) (a) Mokari, T.; Banin, U. *Chem. Mater.* **2003**, *15*, 3955−3960. (b) Manna, L.; Scher, E. C.; Li, L. S.; Alivisatos, A. P. *J. Am. Chem. Soc.* **2002**, *124*, 7136−7145.
(12) Hsu, Y. J.; Lu, S. Y. *Chem. Commun.* **2004**, *18*, 2102−2103.
(13) Wang, Z. L.; Dai, Z. R.; Gao, R. P.; Bai, Z. G.; Gole, J. L. *Appl. Phys. Lett.* **2000**, *77*, 3349−3351.
(14) Hu, J. Q.; Bando, Y.; Liu, Z. W.; Sekiguchi, T.; Golberg, D.; Zhan, J. H. *J. Am. Chem. Soc.* **2003**, *125*, 11306−11313.
(15) He, R. R.; Law, M.; Fan, R.; Kim, F.; Yang, P. D. *Nano Lett.* **2002**, *2*, 1109−1112.
(16) Zhan, J. H.; Bando, Y.; Hu, J. Q.; Sekiguchi, T.; Golberg, D. *Adv. Mater.* **2005**, *17*, 225−230.
(17) Teo, B. K.; Li, C. P.; Sun, X. H.; Wong, N. B.; Lee, S. T. *Inorg. Chem.* **2003**, *42*, 6723−6728.
(18) An, S. J.; Park, W. I.; Yi, G. C.; Kim, Y. J.; Kang, H. B.; Kim, M. *Appl. Phys. Lett.* **2004**, *84*, 3612−3614.

of ZnO and SnO_2 with a heterojunction structure behaved with excellent physical and chemical properties superior to their individual materials.[19] Although many epitaxial heterostructures concerning either ZnO[18,20−24] or SnO_2[15,25] have been obtained successfully, no study regarding a heterostructure with an epitaxial relation between ZnO and SnO_2 was reported up to date. The reason might be ascribed to the apparently striking difference between their crystal structures: ZnO belongs to a hexagonal wurtzite structure (a =3.249 Å and c = 5.206 Å), whereas SnO_2 is a tetragonal rutile structure (a = 4.737 Å and c = 3.186 Å). Note that the oxygen atoms take a hexagonal closest-packed structure in the wurtzite ZnO along the c-axis, and they take a pseudo-hexagonal closest-packed structure in the rutile SnO_2 along the a-axis, resulting in certain crystallographic comparability for some special crystal planes of wurtzite and rutile structures. Thus, it is feasible to fabricate a ZnO/SnO_2 heterostructure with an epitaxial relation.

Herein, we report a rational coupled technique based on chemical vapor deposition for the preparation of the ZnO/SnO_2 heterostructure consisting of a tetrapod-like (T-) ZnO core and a SnO_2 shell, denoted as T-ZnO/SnO_2 core−shell heterostructure. It is found for the first time that the SnO_2 shell has a special epitaxial relation in three dimensions with the ZnO tetrapod substrate. Excitingly, this T-ZnO/SnO_2 epitaxial heterostructure represents unique luminescence properties in contrast with the individual T-ZnO and T-SnO_2 nanostructures. We expect that the T-ZnO/SnO_2 heterostructure could be a remarkable example of tailoring optical properties by the crystal epitaxy.

2. Experimental Section

2.1. Experimental Apparatus. The epitaxial core−shell heterostructure reported here was synthesized in a homemade experimental apparatus where silicon wafers acted as the deposition substrate and heat resource by a direct current (DC) through the silicon wafers instead of a conventional furnace during the deposition of materials. Figure 1a shows the schematic diagram of the experimental apparatus which consists of a horizontal quartz reaction chamber (ϕ 5 cm × 40 cm), silicon substrates, a DC controller, a gas supply and control system, and a rotary pump system. The n-type Si(100) wafers (2 cm × 0.5 cm × 0.03 cm) were ultrasonically cleaned with acetone and then fixed to the sample holder. Silicon substrates were heated to the desired reaction temperature from room temperature within several seconds by adjusting the DC through the silicon wafers. An infrared radiation thermometric indicator (Thermalert TX, Raytek) was used to detect the temperature of the silicon substrate.

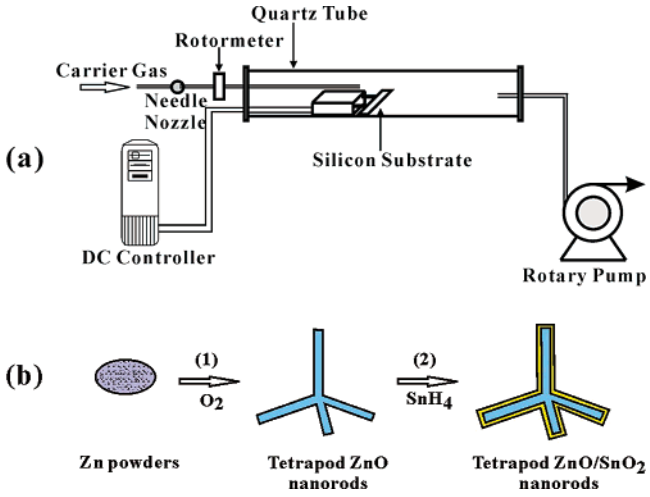

Figure 1. (a) Schematic diagram of the experimental apparatus and (b) a two-step deposition strategy applied to fabricate the T-ZnO/SnO_2 core−shell heterostructure using T-ZnO nanorods as a template.

2.2. Materials Preparation. The deposition procedure involves (1) the preparation of T-ZnO nanorods and (2) subsequent growth of a single-crystal SnO_2 shell as shown in Figure 1b. In a typical synthetic procedure, zinc powder (99.5%) was placed on a silicon wafer for heating while another silicon wafer was placed 5 mm above as the substrate to collect ZnO products. The deposition substrate and the heating silicon wafer were successively heated to about 675 °C and 800 °C within several seconds. A layer of white fluffy product (T-ZnO product) was deposited on the surface of the upper silicon substrate, accompanying the yellow-green flare. At the subsequent deposition step, the precursor SnH_4 was preprepared according to ref 26 and stored in the air pocket (SY-42, Sanhe Medical Instrument Co., Ltd) after being mixed with N_2 at a fixed ratio (8%). After evacuating the reaction chamber to 1−2 Torr, the as-grown T-ZnO on the silicon substrate was heated to the desired temperature (typically T = 770 °C), and then the SnH_4/N_2 mixture was introduced by keeping a flow rate of 60 sccm (standard cubic centimeters per minute). The whole deposition time usually took 5−30 min. The products, T-ZnO/SnO_2 core−shell heterostructures, were converted to SnO_2 hollow nanostructures via further erosion treatment in 0.1 M HCl aqueous solution under ultrasonic action for 4 h. The collected product was washed several times with distilled water and ethanol and then dried at 70 °C.

2.3. Material Characterization. The morphology and structure of the products were characterized by X-ray diffraction (XRD, Rigaku DMAX/rC) with Cu Kα radiation, field emission scanning electron microscopy (FE-SEM, LEO1530) equipped with energy dispersion spectroscopy (EDS), transmission electron microscopy (TEM, Hitachi H600), and high-resolution TEM (HRTEM, TECNAI F-30). The elemental mapping was performed using a Gatan image filtering (GIF) system attached to the F30 HRTEM. Photoluminescence (PL) was measured at room temperature with a Hitachi luminescence spectrometer (F-4500) using a Xenon discharge lamp as the excitation light source, and the excited wavelength was 325 nm. The room-temperature cathodoluminescence (CL) spectra and images were taken using CL system (Gatan, MonoCL) equipped on a high-resolution SEM (FEI, Quanta 200F).

(19) (a) Costello, B. P. J. D.; Ewen, R. J.; Jones, P. R. H.; Ratcliffe, N. M.; Wat, R. K. M. *Sens. Actuators B* **1999**, *61*, 199−207. (b) Belliard, F.; Connor, P. A.; Irvine, J. T. S. *Solid State Ionics* **2000**, *135*, 163−167. (c) Tennakone, K.; Bandara, J. *Appl. Catal., A* **2001**, *208*, 335−341. (d) Bandara, J.; Tennakone, K.; Jayatilaka, P. P. B. *Chemosphere* **2002**, *49*, 439−445. (e) Wang, C.; Zhao, J. C.; Wang, X. M.; Mai, B. X.; Sheng, G. Y.; Peng, P. A.; Fu, J. M. *Appl. Catal., B* **2002**, *39*, 269−279.
(20) Wang, X. D.; Gao, P. X.; Li, J.; Summers, C. J.; Wang, Z. L. *Adv. Mater.* **2002**, *14*, 1732−1734.
(21) Hwang, J.; Min, B. D.; Lee, J. S.; Keem, K.; Cho, K.; Sung, M. Y.; Lee, M. S.; Kim, S. *Adv. Mater.* **2004**, *16*, 422−424.
(22) (a) Heo, Y. W.; Abernathy, C.; Pruessner, K.; Sigmund, W.; Norton, D. P.; Overberg, M.; Ren, F.; Chisholm, M. F. *J. Appl. Phys.* **2004**, *96*, 3424−3428. (b) Saitoh, H.; Okada, Y.; Ohshio, S. *J. Mater. Sci.* **2002**, *37*, 4597−4602.
(23) Wang, X. D.; Summers, C. J.; Wang, Z. L. *Adv. Mater.* **2004**, *16*, 1215−1218.
(24) Bae, S. Y.; Seo, H. W.; Choi, H. C.; Park, J.; Park, J. *J. Phys. Chem. B* **2004**, *108*, 12318−12326.
(25) Gao, T.; Wang, T. H. *Chem. Commun.* **2004**, *22*, 2558−2559.

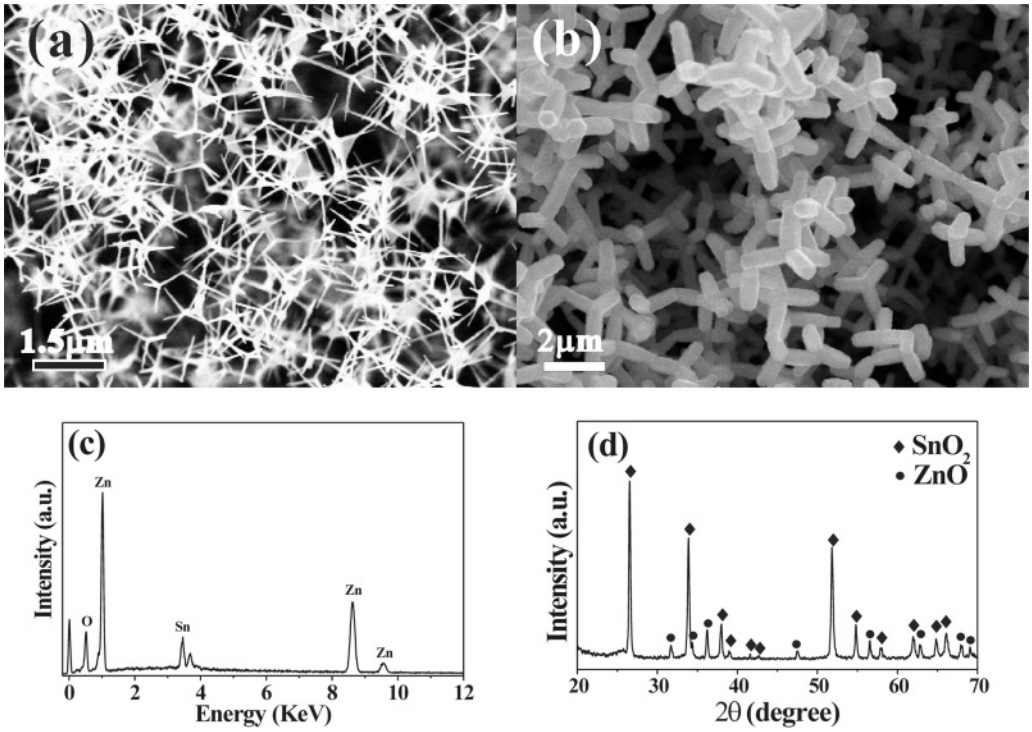

Figure 2. (a) SEM image of the T-ZnO nanostructures obtained at the first deposition step. (b) SEM image of the T-ZnO/SnO_2 core−shell heterostructure obtained after the second deposition step. (c) EDS analysis and (d) the XRD pattern of the T-ZnO/SnO_2 core−shell heterostructure. The diffraction peaks in (d) show the coexistence of the wurtzite ZnO (marked with ●) and rutile SnO_2 (marked with ◆).

3. Results and Discussion

3.1. Morphologies and Composition of the Products. Figure 2a and b show typical SEM images of the morphologies of the products obtained at the first and second deposition steps, respectively. The products obtained via the deposition from Zn (the first deposition step) were uniform tetrapod-like ZnO (T-ZnO) nanorods with good quality and high yield (Figure 2a), which was wurtzite ZnO as characterized by XRD. The diameters of four legs were from 30 to 80 nm, and their lengths were in the range 200−800 nm. After the deposition of SnO_2 (the second deposition step), most of the products still retained initial tetrapod structure, and even their four legs held the hexagonal shape of ZnO nanorods. However, the diameters of the four legs increased markedly, ranging from about 100 nm to several hundreds of nanometers (Figure 2b) depending on the deposition time. The EDS spectrum (Figure 2c) taken from the tetrapod nanostructure of the second deposition step indicated the presence of element Sn besides elements Zn and O. The XRD measurement verified that there was a new phase in addition to wurtzite ZnO (JCPDS 36-1451) as shown in Figure 2d, which could be indexed to the tetragonal rutile structure of SnO_2 (JCPDS 41-1445). No characteristic peak of impurity, such as SnO or Zn_2SnO_4, was observed. As SnH_4 decomposes rapidly at high temperature,[26,27] the authentic process in the second deposition step ($T = 750$ °C) should be attributed to the reaction of the precursor SnH_4 with residual oxygen in the reaction chamber as the following equations: $SnH_4 \rightarrow Sn + H_2$, $Sn + O_2 \rightarrow SnO_2$,[26] further forming continuous SnO_2 films on the surfaces of T-ZnO nanorods.

Figure 3a−d show a scanning transmission electron microscopy (STEM) image of a T-ZnO/SnO_2 nanostructure and the corresponding elemental maps of O, Zn, and Sn concentrations. It is clearly seen that element O was distributed uniformly in the whole tetrapod nanorods, element Zn was mainly located in the core, and yet element Sn was mainly located in the outer layer of the tetrapod structure. Analysis of the cross-sectional composition line profiles (Figure 3e) showed that ZnO core was about 60−70 nm and the outer SnO_2 layer was about 15−30 nm. The above results demonstrate unambiguously the successful preparation of the T-ZnO/SnO_2 core−shell heterostructures.

3.2. Epitaxial ZnO/SnO_2 Heterostructure. 3.2.1. Epitaxial Relation between ZnO Core and SnO_2 Shell. The microstructures of the interface between the ZnO core and the SnO_2 shell were investigated by HRTEM and selective area electron diffraction (SAED). Figure 4a is a low-magnification HRTEM image of a single nanorod of a T-ZnO/SnO_2 heterostructure, which clearly shows that the ZnO nanorod was completely coated with a well-crystallized SnO_2 layer. The SnO_2 layer was not flat, having a wavy surface with a periodic variation of 20−40 nm. A deep insight of the magnified HRTEM image showed a Moiré pattern with a periodicity of about 3.7 nm in the core region due to the overlapping of different crystal lattices of ZnO and SnO_2.[28] The corresponding SAED pattern (Figure 4b) revealed two sets of diffraction patterns (marked with yellow cycles and red cycles), respectively corresponding to the wurtzite ZnO $[2\bar{1}\bar{1}0]$ zone axis pattern and the rutile SnO_2 [001] zone axis pattern. The SAED patterns observed in different orientations and different samples showed the same and unique relationship between the crystal structures of the ZnO core and SnO_2 shell, i.e., $(010)_{SnO_2}||(0\bar{1}10)_{ZnO}$ and $[100]_{SnO_2}||[0001]_{ZnO}$, respectively. It ought to be noted that the spacing between (100) planes of SnO_2 was calculated to be 0.485 nm from the SEAD pattern by self-calibrating the $d_{ZnO-(0001)}$ to the standard value of 0.521 nm, larger than the bulk value of 0.478 nm, which revealed an expansion of the SnO_2 unit cell in the *a*-axis. Such a lattice expansion is also consistent with the periodicity of the observed Moiré pattern, which can be calculated by the lattice mismatching[28] between the core and the shell according to $D = (d_1{*}d_2)/(d_1 - d_2) = 3.5$ nm, where $d_1 = d_{ZnO-(0002)} = 0.2605$ nm, $d_2 = d_{SnO_2-(200)} = 0.2425$ nm.

Figure 4c is a magnified HRTEM image taken from the area "c" in Figure 4a, which depicts the interface structure between the ZnO core

(26) Wang, C. F.; Xie, S. Y.; Lin, S. C.; Cheng, X.; Zhang, X. H.; Huang, R. B.; Zheng, L. S. *Chem. Commun.* **2004**, *15*, 1766−1767.
(27) Tamaru, K. *J. Phys. Chem.* **1956**, *60*, 610−612.
(28) Hirsch, P.; Howie, A.; Nicholson, R. B.; Pashley, D. W.; Whelan, M. J. *Electron microscopy of thin crystals*; Robert E. Krieger Publishing: Malabar, FL, 1977.

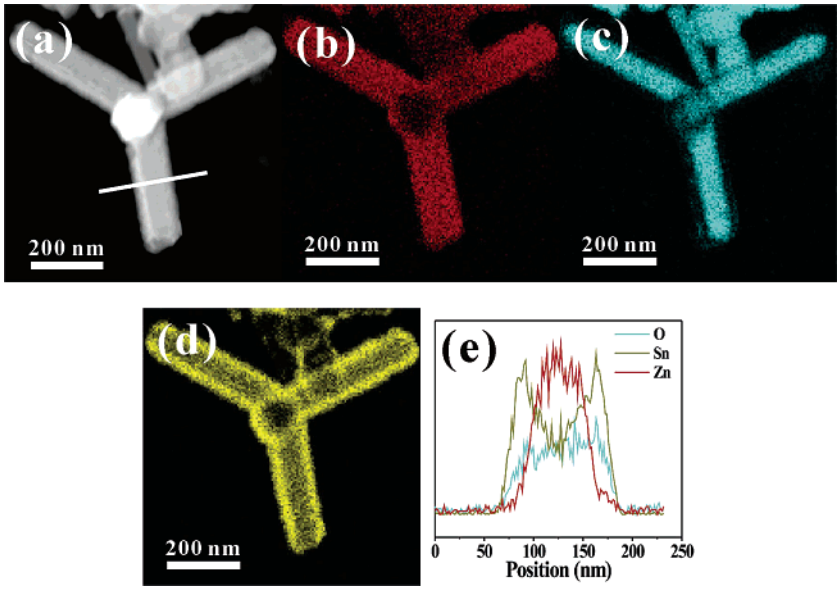

Figure 3. (a) STEM image of T-ZnO/SnO_2 core−shell heterostructure. (b−d) Elemental maps of O, Zn, and Sn concentrations in the T-ZnO/SnO_2 heterostructure, respectively. (e) Cross-sectional compositional line profiles of a ZnO/SnO_2 nanorod (indicated by a line in Figure 3a).

and epitaxial SnO_2 shell. Both the ZnO core and the SnO_2 shell exhibit clear lattice fringes separating each other with an atomically sharp interface, indicating the epitaxial growth of the SnO_2 shell. The spacing between two adjacent lattice planes in the core region is close to 0.520 nm and consistent with the (0001) planes of wurtzite ZnO. On the other hand, the SnO_2 shell has a clear quasi-square fringe, principally corresponding to the (100) planes of rutile SnO_2, whereas the interlayer spacing parallel to the $(0001)_{ZnO}$ plane is slightly larger than that perpendicular to the $(0001)_{ZnO}$ plane so that the interlayer spacings of (100) and its equivalent (010) lattice planes become unequal. Such inequality between lattice spacings of (100) and (010) should be attributed to lattice distortion resulting from lattice mismatch, whereby the in-plane layer lattice parameter is forced to that of the substrate (i.e., 0.52 nm for ZnO), and the out-of-plane lattice parameter distorts according to the Poisson effect.[29] In this paper, we specify the two inequivalent {100} planes of SnO_2 shell as the $(100)_{SnO_2}$ plane for that parallel to $(0001)_{ZnO}$ plane and $(010)_{SnO_2}$ planes for that perpendicular to $(0001)_{ZnO}$ plane, respectively. Furthermore, the enlarged image (the inset of Figure 4c) of the interface fringe reveals that there is a perceptible decrease from 0.51 to 0.48 nm for the distance between $(100)_{SnO_2}$ planes from the ZnO/SnO_2 interface to the SnO_2 bulk phase. Such a slight decrease of (100) interlayer spacing should result from the lattice mismatch between the SnO_2 shell and ZnO core, which would inevitably induce the injection of structure defects (such as misfit dislocations) into the SnO_2 shell to release the increasing stress with the thickness of the SnO_2 epitaxial layer. In the present case, misfit dislocations as indicated by an arrow in the Figure 4c were frequently observed in the SnO_2 epitaxial layer, especially in the concave area of the wavy SnO_2 layer. Even in the case of a thinner epitaxial layer (5−10 nm thickness), such misfit dislocations still appeared (Figure 4d).

Structurally, ZnO and SnO_2 belong to two different crystal systems, the hexagonal wurtzite structure (a =3.249 Å and c = 5.206 Å) and tetragonal rutile structure (a = 4.737 Å and c = 3.186 Å). It seems there should be a striking difference between the two types of crystal structures, and it is difficult to fabricate such a ZnO/SnO_2 heterostructure with an epitaxial relation. As a matter of fact, to date, there has been no report about the epitaxy of SnO_2 on ZnO substrate. By carefully analyzing both crystal structures, we demonstrate here the feasibility of heteroepitaxial growth of the crystalline SnO_2 shell on the ZnO core as shown in atomic packing models of Figure 4e. It can be seen that the atomic arrangements of the $(010)_{SnO_2}$ plane have very good structural compatibility with that of the $(0\bar{1}10)_{ZnO}$ plane. The lattice (O−O distance) mismatches along the $[2\bar{1}\bar{1}0]_{ZnO}$ and $[0001]_{ZnO}$ directions are only 1.8% and 8.8%, respectively. Therefore, epitaxy of the SnO_2 shell on the ZnO substrate is possible. However, along the $[0001]_{ZnO}$ direction, the lattice mismatch is relatively large, and therefore many misfit dislocations exist in order to release the strain. This could also explain the formation of the wavy SnO_2 surface along the $[0001]_{ZnO}$ directions.

3.2.2. Three-Dimensional Epitaxy of SnO_2 Shell on ZnO Core. The above HRTEM results have demonstrated the two-dimensional epitaxial growth for the SnO_2 layer on the ZnO $\{01\bar{1}0\}$ planes. However, the as-prepared ZnO/SnO_2 heterostructure is a tetrapod structure with a hexagonal cross section, rather than a simple plane. The SEAD patterns in different orientations showed that it is a single-crystal SnO_2 shell enveloping a single-crystal ZnO core. To have a deep insight into how a single-crystal SnO_2 shell can epitaxially grow on a ZnO hexagonal core, the T-ZnO/SnO_2 heterostructures were further treated with 0.1 M HCl to obtain hollow SnO_2 shells. Due to the different resistances to the acid erosion between ZnO and SnO_2, the T-ZnO/SnO_2 heterostructures were converted into denucleated SnO_2 tetrapods (notified as T-SnO_2 shell) which remained at a very good crystallinity as shown in Figure 5a. Figure 5b is a HRTEM image of the SnO_2 tube wall, showing a clearly resolved lattice fringe distance $d_{(110)}$ = 0.343 nm, larger than its common value (0.335 nm) due to the expansion of the SnO_2 unit cell in the a-axis. The result agrees well with previous analysis of the structure of SnO_2 epitaxial layer in the T-ZnO/SnO_2 core−shell heterostructure.

In the products after the acid treatment, hexagonal ringlike nanostructures (notified as hexagonal nanorings) were accidentally observed in addition to numerous T-SnO_2 shells as shown in Figure 5c and d. The hexagonal nanorings increased markedly with the increasing time of ultrasonic treatment. The side view (Figure 5c) shows that the height of the hexagonal nanoring is 20−40 nm, being well consistent with the periodicity of the wavy surface. The top view (Figure 5d) reveals that internal diameter of hexagonal nanoring is about 80−100 nm, and the wall thickness is about 15−30 nm, consistent with the SnO_2 epitaxial shell in the T-ZnO/SnO_2 heterostructure. Therefore, the hexagonal nanorings are apparently cloned from the hexagonal shape of the ZnO nanorods. Associated with the wavy surface of the SnO_2 epitaxial shell having a periodicity of 20−40 nm (see Figure 4a) and the possible existence of lattice misfit dislocations in the concave area, it is believed

(29) Hull, R.; Gray, J.; Wu, C. C.; Atha, S.; Floro, J. A. *J. Phys.: Condens. Matter* **2002**, *14*, 12829−12841.

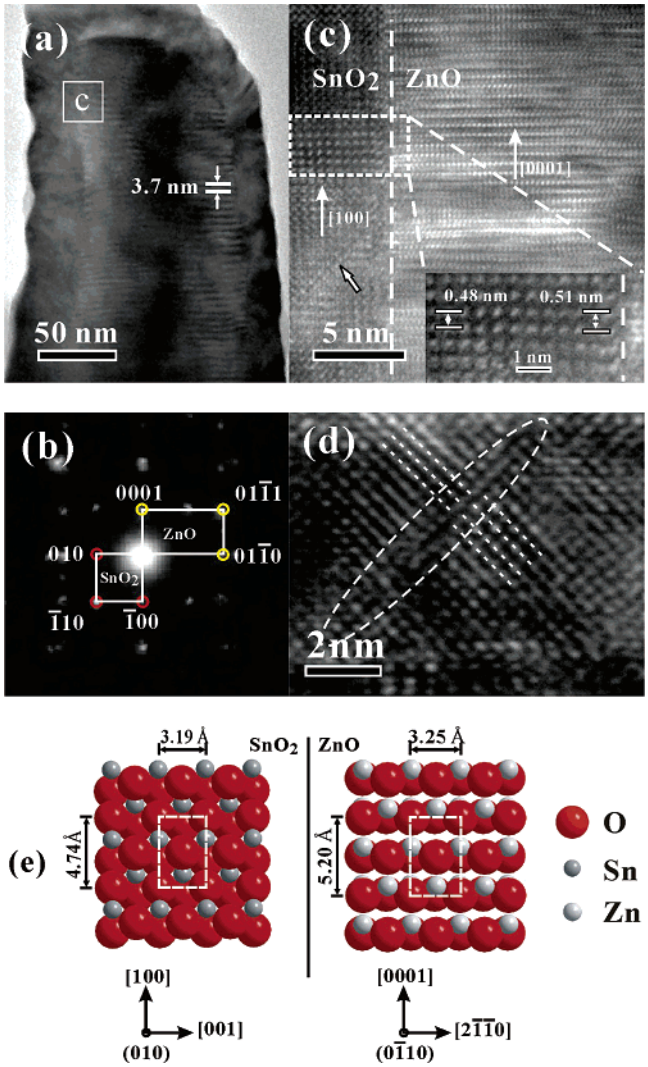

Figure 4. (a) Low-magnification TEM image of a single nanorod of a tetrapod ZnO/SnO_2 heterostructure. (b) The corresponding SAED pattern of the single nanorod. (c) HRTEM image recorded from the area "c" indicated in (a). The inset is a magnified image of the crystal fringes in the SnO_2 shell. (d) HRTEM image of misfit dislocations in the SnO_2 epitaxial layer. (e) Schematic models of the atomic arrangements on the epitaxial $(010)_{SnO2}$ plane and $(0\bar{1}10)_{ZnO}$ plane.

that these hexagonal nanorings are likely to be broken apart from the SnO_2 epitaxial shell of the ZnO/SnO_2 core−shell heterostructure under the intensive ultrasonic action when the ZnO nanorod core is dissolved in HCl solution. Figure 5e is a typical HRTEM image of a corner of the SnO_2 hexagonal nanoring. Both sides I and II exhibit clear fringes, and their interlayer spacings are about 0.274 nm, being indexed as {101} lattice planes of rutile SnO_2. The inset shows the corresponding fast Fourier transform (FFT) pattern, which corresponds to the pattern of a [100] zone axis. It should be noticed that all diffraction spots are obviously split into two sets, indicating a small orientation difference of the lattices in sides I and II of the SnO_2 nanoring. Actually, detailed analysis of the HRTEM image also reveals that there is a misorientation of about 7°−8° between {101} planes of sides I and II. In addition, as shown in the corresponding inverse-FFT image in Figure 5f, edge dislocations were clearly observed in the lattice fringes near the corner.

Figure 6 shows a schematic model of the SnO_2 hexagonal nanoring surrounding the ZnO hexagonal nanorods with epitaxial growth of $(010)_{SnO_2}$ lattice planes on all the six $\{0\bar{1}10\}$ surfaces of a ZnO hexagonal nanorod. The model is projected from the [0001] direction of the ZnO core and partially drawn. The theoretical misorientation between {101} planes of sides I and II is 7.8°, agreeing well with the experimental value. Theoretically, the SnO_2 shell (hexagonal nanoring) can be formed by either a polycrystalline mode or a single-crystal mode. For the polycrystalline mode, six SnO_2 crystallites independently grow on the six side surfaces of the ZnO nanorod, and then grain boundaries are left in the corner of the SnO_2 hexagonal nanoring because of the geometric mismatch between the SnO_2 and ZnO crystals. In fact, only some edge dislocations instead of grain boundaries were observed in the corner region. The result indicates that the epitaxial growth of SnO_2 shell takes single-crystal mode where the whole hexagonal shell is a single crystal, and the misorientation of 7.8° between (101) planes is compensated by introducing edge dislocations into the fringes near the corner (see Figure 5e, f). In a way, structural comparability of SnO_2 and ZnO is an intrinsical and key factor to allowing the epitaxial growth take the single-crystal mode rather than the polycrystalline mode. It is known that the O atoms in the $(0001)_{ZnO}$ plane take a hexagonal closest-packed arrangement, having a 6-fold symmetry. As for the $(100)_{SnO_2}$ plane surrounding ZnO nanorods, O atoms take a pseudo-hexagonal closest-packed arrangement, having a quasi-six-fold symmetry. Taking account of the very small lattice mismatch (only 1.8%) in the $[001]_{SnO_2}||[2\bar{1}\bar{1}0]_{ZnO}$ direction (the horizontal direction), it is reasonable to conclude that as long as stacking oxygen atoms appreciably adjust the arrangement in the crystal structure, the SnO_2 epitaxial layer can easily overcome the misorientation in the corner and encloses ZnO nanorods to form a close and single-crystal hexagonal epitaxial ring.

All these results, when combined, not only explain the planar epitaxial growth of SnO_2 layer on $\{0\bar{1}10\}_{ZnO}$ substrate surface but also demonstrate how the SnO_2 epitaxial shell grows across the different substrate surfaces of the ZnO hexagonal prism to form a close single-crystal epitaxial shell. Such complicated epitaxy between the tetrapod ZnO core and SnO_2 shell is quite different from the planar epitaxy as in the cases of epitaxial films[30] and biaxial nanocables.[15] In the past cases, although a few epitaxial layers have been grown on complicated surfaces, such as forming Ge/Si[8] or ZnO/GaN[18] epitaxial core−shell nanowires/nanorods, such complicated epitaxy only occurs between those materials with the same crystal system up to now. The present study here opens a road to establishing new types of complicated epitaxial layers constructed with different crystal structures.

3.3. Optical Properties of Core−Shell ZnO/SnO_2 Structures. Figure 7a shows the room-temperature PL spectrum of four types of the products. Before SnO_2 coating, the T-ZnO nanorods have only a strong ultraviolet (UV) emission with a peak at 380 nm, which corresponds to the near band edge (NBE) peak, being responsible for the recombination of free excitons of ZnO.[31] After the coating of SnO_2, the T-ZnO/SnO_2 heterostructure exhibits a luminescence property quite different from that of T-ZnO nanorods. Besides the UV emission of ZnO with a peak at 380 nm, a shoulder peak at 398 nm and a broad green emission centered at 500 nm in the wavelength range 450−600 nm are observed. The PL spectrum of the T-SnO_2 shell shows a peak at about 398 nm, and there is no peak in the range 450−600 nm, indicating that the shoulder peak at 398 nm for the T-ZnO/SnO_2 heterostructures comes from photoluminescence of the SnO_2 shell.[32]

The green emission of 450−600 nm is usually believed to be related to the intrinsic defect structures, in particular the oxygen vacancies originated from the oxygen deficiency.[33] To confirm the origin of the broad green emission from T-ZnO/SnO_2 core−shell heterostructures,

(30) (a) Fons, P.; Iwata, K.; Niki, S.; Yamada, A.; Matsubara, K. *J. Cryst. Growth* **1999**, *201/202*, 627−632. (b) Fons, P.; Iwata, K.; Yamada, A.; Matsubara, K.; Niki, S.; Nakahara, K.; Tanabe, T.; Takasu, H. *Appl. Phys. Lett.* **2000**, *77*, 1801−1803. (c) Zeuner, A.; Alves, H.; Hofmamn, D. M.; Meyer, B. K.; Heuken, M.; Bläsing, J.; Krost, A. *Appl. Phys. Lett.* **2002**, *80*, 2078−2080. (d) Kimura, H.; Fukumura, T.; Koinuma, H.; Kawasaki, M. *Physica E* **2001**, *10*, 265−267.
(31) Chen, Y. F.; Bagnall, D. M.; Koh, H. J.; Park, K. T.; Hiraga, K.; Zhu, Z. Q.; Yao, T. *J. Appl. Phys.* **1998**, *84*, 3912−3918.
(32) Gu, F.; Wang, S. F.; Lü, M. K.; Zhou, G. J.; Xu, D.; Yuan, D. R. *J. Phys. Chem. B* **2004**, *108*, 8119−8123.
(33) (a) Dai, Y.; Zhang, Y.; Li, Q. K.; Nan, C. W. *Chem. Phys. Lett.* **2002**, *358*, 83−86. (b) Vanheusden, K.; Warren, W. L.; Seager, C. H.; Tallant, D. R.; Viogt, J. A.; Gnade, B. E. *J. Appl. Phys.* **1996**, *79*, 7983−7990.

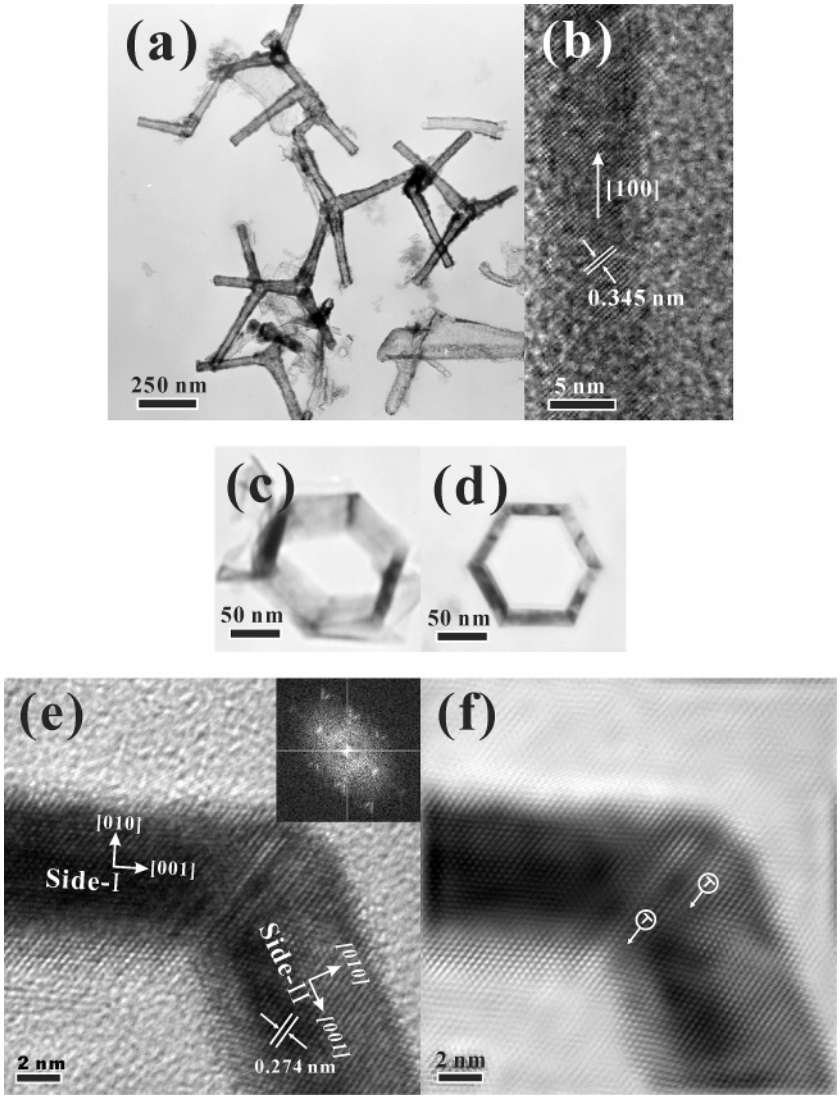

Figure 5. (a) Low-magnification TEM image of large quantities of T-SnO_2 shell obtained via the acid corrosion. (b) HRTEM image of the wall of the T-SnO_2 shell. (c and d) Low-magnification TEM images displaying the hexagonal shape from various views of the SnO_2 nanoring obtained via intensive ultrasonic treatment for 4h. (e and f) HRTEM image and corresponding inverse-FFT image of a corner of a SnO_2 hexagonal nanoring.

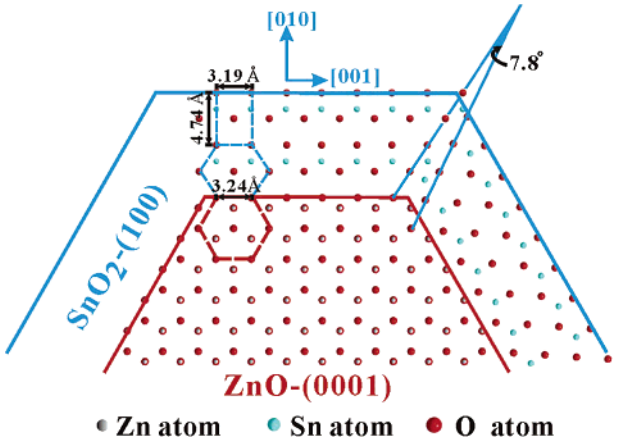

Figure 6. Schematic model of the SnO_2 hexagonal nanoring surrounding a ZnO nanorod. Red section displays atom arrangement on the (0001) plane of a ZnO core, and blue section displays atom arrangement on the (100) plane of the SnO_2 epitaxial shell.

the PL spectrum of T-ZnO nanorods annealed in the identical deposition condition was measured. It is found that a faint green emission at about 450−600 nm appears in the annealed T-ZnO nanorods, but much lower than that of ZnO/SnO_2 heterostructures. The faint green emission of annealed T-ZnO nanorods can be attributed to the generation of oxygen vacancies during the annealing in the oxygen deficient atmosphere. However, it does not fully account for the obvious enhancement of the green light emission after T-ZnO nanorods are coated by the SnO_2 shell. As there is no similar emission from the denucleated T-SnO_2 shells or the mechanical mixture of the T-ZnO core and denucleated T-SnO_2 shells, the green emission should be also correlated with the epitaxial heterojunction structure in T-ZnO/SnO_2 nanostructures.

Direct evidence of the origin of such green emissions arose from the CL spectra and images at room temperature (see Figure 7b). In accord with PL results, the T-ZnO/SnO_2 heterostructures represent two main emission bands in the CL spectrum. The NBE peak of ZnO appears at 382 nm, while the green emission is shifted to 524 nm. Different from the PL spectrum, the intensity of NBE emission in T-ZnO/SnO_2 heterostructures decreases, while the intensity of the green emission is significantly enhanced, even stronger than the former. More useful information about the contribution of two emissions is provided by their monochromatic CL images (the insets of Figure 7b). As shown in the images, the T-ZnO nanorods emit very strong UV light (380 nm, inset 1 of Figure 7b). For a T-ZnO/SnO_2 heterostructure, the UV light is localized in the T-ZnO core region (inset 2 of Figure 7b). However, the monochromatic CL image at a wavelength of 524 nm

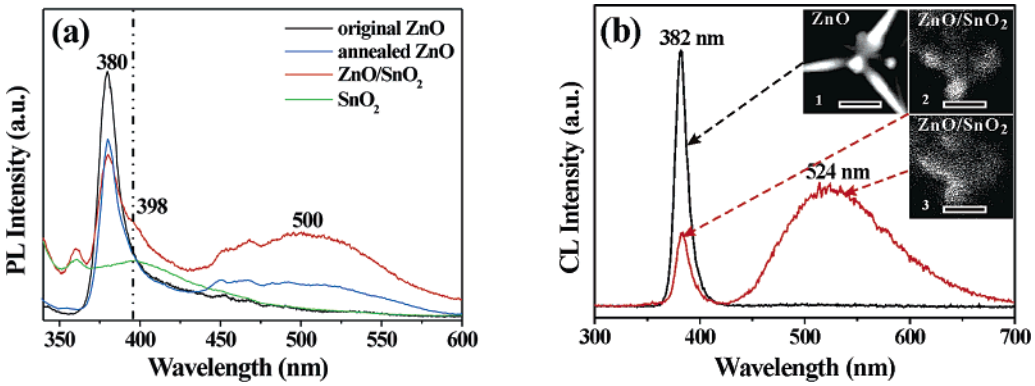

Figure 7. (a) Room-temperature PL spectra of original T-ZnO nanorods, annealed T-ZnO nanorods, T-ZnO/SnO_2 core−shell heterostructures, and T-SnO_2 shell. The excitation wavelength was 325 nm. (b) Room-temperature CL spectra of original T-ZnO nanorods and T-ZnO/SnO_2 core−shell heterostructures. The insets are the monochromatic CL images at 382 nm (for 1 and 2) and 524 nm (for 3) emission, respectively. The scale bar is 500 nm.

(inset 3 of Figure 7b) for the same T-ZnO/SnO_2 heterostructure clearly shows that the green light was sent out from the whole region of T-ZnO/SnO_2 heterostructures. Therefore, the green light is not localized in the ZnO core or the epitaxial interfaces such as other ZnO heterostructures reported in the previous study.[24] In other words, the epitaxial heterojunction structure may have induced a new type of emission over the whole region of T-ZnO/SnO_2 heterostructures, although the oxygen vacancies in the ZnO core and defects or strain in the interfacial area introduced by the epitaxial growth of SnO_2 may result in the green emission. Although the more detailed mechanism of the source of such green emission in the as-prepared T-ZnO/SnO_2 heterostructures is still under investigation, the preliminary results have implied a successful tailoring of the optical properties.

Up to now, many methods have been developed to tailor or tune the luminescence of the semiconductor, including doping with luminescent activators,[34] modifying the surface,[35] and forming a core−shell structure by coating with other luminescent materials.[36] However, not enough attention was attached to the function of the interface in the heterostructures in the previous studies.[24] We believe that the present study would provide a new way to tailor optical properties of semiconductors and might inspire more interest in the influence of the interfacial region on the device properties.

3.4. Influence of Reaction Conditions on the Morphology of SnO_2 Shells. Since epitaxial growth always takes place under nonequilibrium conditions, the control of growth kinetics is of high importance to heteroepitaxy like the ZnO/SnO_2 system, which affects profoundly the thickness and quality of the epitaxial layer. In our experiments, reaction temperature, deposition time, and other experimental factors including carrier gas (concentration and flow rate) and the system pressure need to be controlled properly to obtain well-grown core−shell nanostructures during the second deposition process. It was found that the diameter of nanorods of tetrapod nanocomposites increased from about 130 to 780 nm along with the deposition time from 5 to 20 min (see Figure 8a−c) (typically, $T = 770$ °C, flow rate = 60 sccm). At the same time, the surface of the nanorods became highly coarse, even attached many SnO_2 nanoparticles when the deposition time exceeds 20 min (Figure 8c), which indicated that an excessively long deposition time did not favor the growth of the single-crystal SnO_2 shell. The prime reason might be that the stress increases with the increasing thickness of the epitaxial film so that the subsequent growth of SnO_2 atoms tends to nucleate and form small particles. The reaction temperature is another important factor in the epitaxial growth of SnO_2 on the surface of ZnO nanorods. As shown in Figure 8d, when the reaction temperature was relatively low (630 °C), the SnO_2 shell formed epitaxial islands rather than a continuous single-crystal film on the surface of T-ZnO nanorods. With the increase of the reaction temperature (see Figure 8e, 8a), the crystallinity of the SnO_2 shell was improved markedly because of the high mobility of deposited atoms on the surface at high substrate temperature. Through a series of experiments, the optimized conditions for heteroepitaxial growth of SnO_2 on T-ZnO nanorods in our apparatus is a 750−800 °C reaction temperature, 5−10 min deposition time, and a 60 sccm flow rate of mixture gas (8% concentration).

It is well-known that ZnO nanostructures have very rich morphologies. Among the diverse ZnO nanostructures, T-ZnO nanostructure holds a complicated structure comprising four nanorods and thus is a very good template for demonstrating the versatility of our two-step deposition route to fabricate SnO_2 epitaxial shells on various ZnO cores. Preliminary results have shown the possible preparation of aligned ZnO/SnO_2 nanocable arrays and denucleated SnO_2 nanotube arrays on the silicon substrate by our proposed method, and further studies on their properties and other ZnO/SnO_2 nanostructures are in progress.

4. Summary

The epitaxial T-ZnO/SnO_2 core−shell heterostructure has been synthesized for the first time via a two-step deposition process based on the chemical vapor deposition technique. The as-synthesized materials still kept the same shape with the initial ZnO template, and the denucleated T-SnO_2 shells were also successfully obtained through further treatment by HCl solution. The structural characterizations reveal that a good epitaxial relationship existed between the wurtzite ZnO core and the nearly single-crystal rutile SnO_2 shell. Based on investigation of the compatibility of atomic arrangement in crystal lattices, a rational model is proposed to explain the feasibility of such novel epitaxial growth between the wurtzite ZnO substrate and the rutile SnO_2 shell through lattice distortions and structure defects such as misfit dislocations. Excitingly, the as-synthesized T-ZnO/SnO_2 heterostructure exhibited unique luminescence properties in contrast with individual T-ZnO nanorods and the T-SnO_2 shell, where a new emission induced by the epitaxial interface was observed.

Epitaxial ZnO/SnO_2 heterostructures presented here may have extended the heteroepitaxial family, and they also provide opportunities for the study of the fundamental properties of the

(34) (a) Gu, F.; Wang, S. F.; Lü, M. K.; Zhou, G. J.; Xu, D.; Yuan, D. R. *Langmuir* **2004**, *20*, 3528−3531. (b) Geng, B. Y.; Wang, G. Z.; Jiang, Z.; Xie, T.; Sun, S. H.; Meng, G. W.; Zhang, L. D. *Appl. Phys. Lett.* **2003**, *82*, 4791−4793. (c) Karvinen, S. M. *Ind. Eng. Chem. Res.* **2003**, *42*, 1035−1043.

(35) (a) Niederberger, M.; Garnweitner, G.; Krumeich, F.; Nesper, R.; Cölfen, H.; Antonietti, M. *Chem. Mater.* **2004**, *16*, 1202−1208. (b) Guo, L.; Yang, S. H.; Yang, C. L.; Yu, P.; Wang, J. N.; Ge, W. K.; Wong, G. K. L. *Chem. Mater.* **2000**, *12*, 2268−2274.

(36) (a) Fu, L.; Liu, Z. M.; Liu, Y. Q.; Han, B. X.; Wang, J. Q.; Hu, P. G.; Cao, L. C.; Zhu, D. B. *J. Phys. Chem. B* **2004**, *108*, 13074−13078. (b) Yang, H.; Holloway, P. H.; Cunningham, G.; Schanze, K. S. *J. Chem. Phys.* **2004**, *121*, 10233−10240.

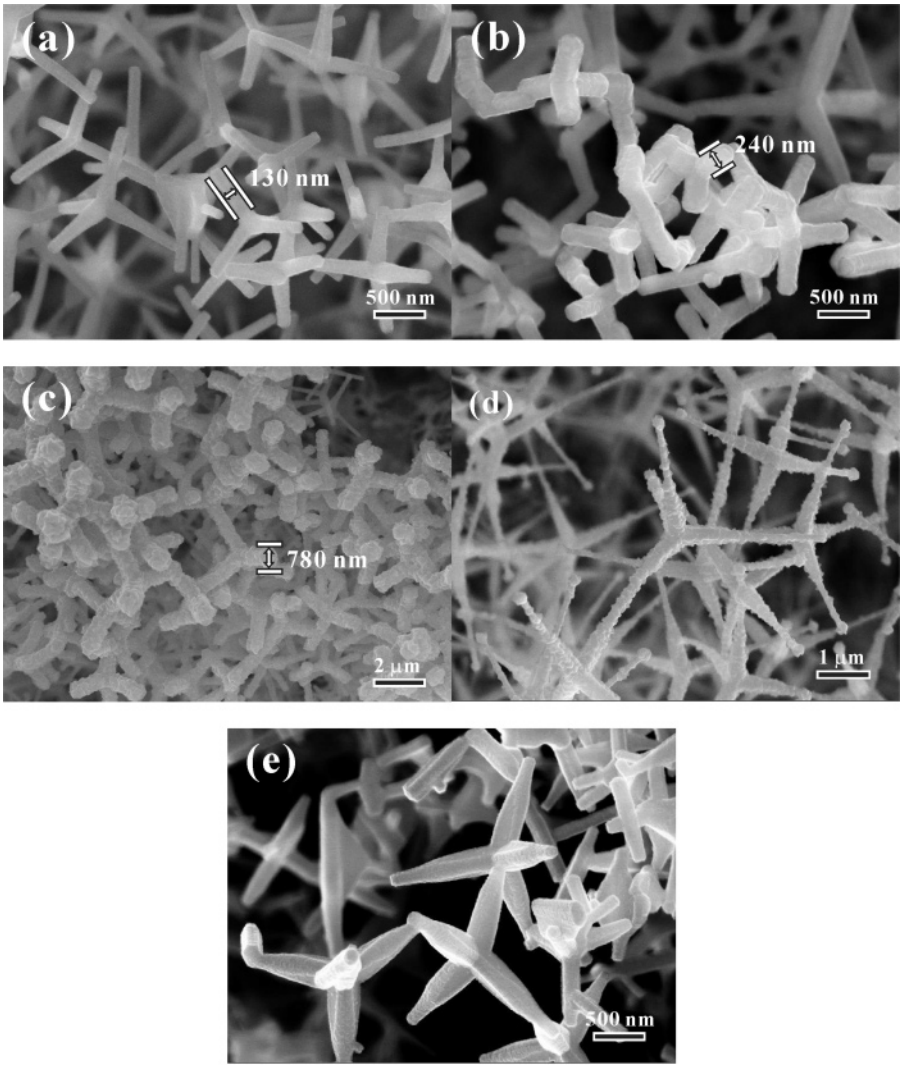

Figure 8. Influences of different experimental conditions on the growth of SnO_2 shells. (a−c) SEM images of the products obtained at the different deposition times (corresponding to 5, 10, and 20 min, respectively), while keeping the deposition temperature at 770 °C. (d and e) SEM images of the products obtained at the deposition temperatures of 630 °C and 710 °C, respectively. The deposition time is 5 min.

novel ZnO/SnO_2 heteroepitaxy system. It could be expected that other complicated epitaxy systems and the resulted new properties will be discovered, which would have potential applications in laser, gas sensor, solar energy conversion, photo catalysis, and nanodevices in the future.

Acknowledgment. We thank Prof. Dapeng Yu and Dr. Jun Xu from Peking University Electron Microscopy Laboratory for the CL measurement. This work was supported by the National Natural Science Foundation of China (Grant Nos. 20021002, 20273052, and 20473069), the Ministry of Science and Technology of China (Grant No. 2001CB610506), NCET from the Ministry of Education of China, and the Fok Ying-Tung Educational Foundation.

JA052259T